

Article

Mathematical Simulation of Iron Ore Fines Sintering Process with Solid Fuel Segregation Distribution and Corresponding Heat Pattern Study

Qiangjian Gao ^{1,2,*}, Lei Bao ^{1,2,*}, Pengxuan Zhu ^{1,2}, Xin Jiang ^{1,2}, Haiyan Zheng ^{1,2}  and Fengman Shen ^{1,2}

¹ Key Laboratory for Ecological Metallurgy of Multimetallic Mineral of Ministry of Education, Northeastern University, Shenyang 110819, China

² School of Metallurgy, Northeastern University, Shenyang 110819, China

* Correspondence: gaoqj@smm.neu.edu.cn (Q.G.); baolei2022112022@126.com (L.B.)

Abstract: The fuel segregation distribution sintering process, with a high fuel dosage in upper layer and a low fuel dosage in bottom layer of the sintering bed, was studied to handle uneven heat distribution problems in the conventional iron ore sintering process. A mathematical simulation method was adopted to contrastively study the fuel segregation distribution sintering process and the conventional iron ore sintering process. The accuracy of the model was verified through the sintering experiments. In addition, different heights of the upper and bottom sintering beds were discussed to assess the fuel segregation distribution sintering technology. In contrast to the conventional iron ore sintering process, the temperature evolution in the sintering bed using the fuel segregation distribution sintering technology tended to be more reasonable and the heat accumulation in the upper bed increased, which meant that the melt quantity index increased from 2178 to 2387 K·min⁻¹, and cooling rate decreased from 360 to 199 K·min⁻¹. The drawbacks of the conventional iron ore sintering process, such as the heat shortage in upper bed and excess heat in lower bed, were therefore improved, which was also proven to promote the sinter quality.

Keywords: iron ore fines sintering; fuel segregation distribution; heat distribution; mathematical simulation



Citation: Gao, Q.; Bao, L.; Zhu, P.; Jiang, X.; Zheng, H.; Shen, F. Mathematical Simulation of Iron Ore Fines Sintering Process with Solid Fuel Segregation Distribution and Corresponding Heat Pattern Study. *Metals* **2022**, *12*, 2126. <https://doi.org/10.3390/met12122126>

Academic Editor: Eric Hug

Received: 14 November 2022

Accepted: 9 December 2022

Published: 11 December 2022

Publisher's Note: MDPI stays neutral with regard to jurisdictional claims in published maps and institutional affiliations.



Copyright: © 2022 by the authors. Licensee MDPI, Basel, Switzerland. This article is an open access article distributed under the terms and conditions of the Creative Commons Attribution (CC BY) license (<https://creativecommons.org/licenses/by/4.0/>).

1. Introduction

The iron ore fines sintering process aims to produce high-strength sinter. It generally involves blending the raw materials containing iron ore, flux, and solid fuel in an agitated mixer, granulating the blends in a roller, charging the granulated materials in the sintering bed, igniting the solid fuel, the gradual approaching of the combusting front towards the bottom of the bed, sintering the iron-bearing materials with the combustion heat together with air-suction beneath the sintering machine, and obtaining the fired sinters and crushing them for the blast furnace (BF) process [1]. A diagram of the iron ore fines sintering process is presented in Figure 1.

A series of physical and chemical processes occur during sintering along with mass and heat transfer [2]. The bed height can be divided into five zones (from top to bottom): fired sinter, combustion, preheating, dry, and damp zones. The details of the division and the corresponding reactions are shown in Figure 2.

As the main iron-bearing material for blast furnace ironmaking, sinter output is maintained at a high level worldwide. For instance, approximate 1.4 billion tons of sinter were consumed in China in 2020 [3]. Therefore, to meet the demands for sinter, improving sinter quality is a major issue. Figure 3 shows the main zones of the conventional sintering process (CS) considering both the bed height y and width x . It can be concluded that when the combustion of fuel propagates downward along with the sintering machine travelling ahead, the heat automatically flows from top to bottom, which results in the accumulation of heat in the bottom layer. This is because the combustion zone enlarges gradually from

top to bottom. Consequently, the heat deficiency in the upper section of the sintering bed and excess heat in the bottom section of that are regarded as the main drawbacks of the CS, which inevitably causes a difference in the sinter quality between the upper and bottom sections of the sintering bed [4].

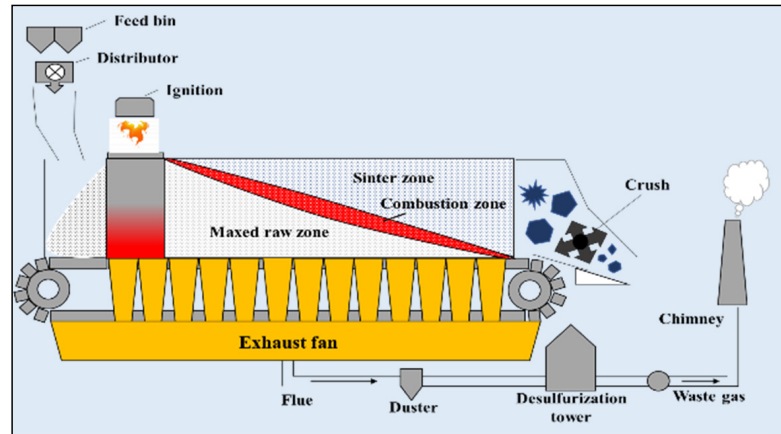


Figure 1. Schematic of the sintering process.

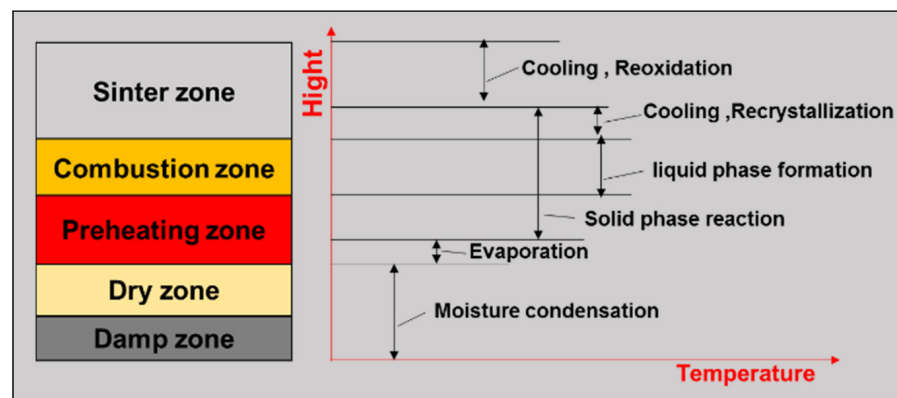


Figure 2. Various zones in the sintering bed in the height direction.

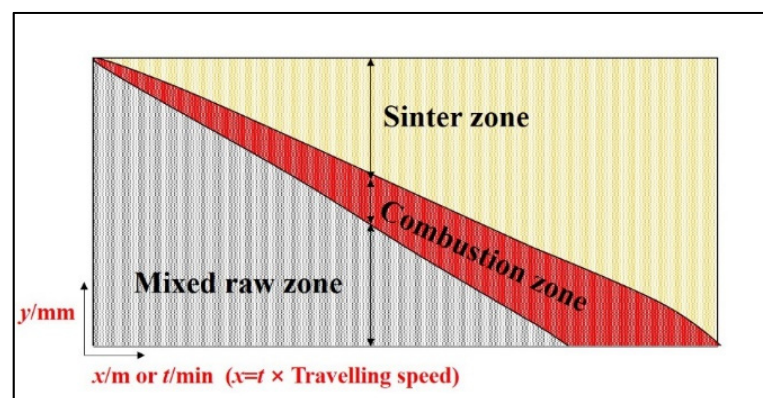


Figure 3. General zone of sintering bed in height and width direction.

To improve the uneven heat distribution in the conventional sintering process, injection of a combustible gas in the iron ore fines sintering process was proposed to optimize energy efficiency. Castro et al. [5] stated that gas injection during iron ore sintering could improve sinter quality and reduce pollutant emissions. Meng et al. [6] established a model to study the gas fuel injection sintering process, and their results confirmed that this technology can enhance the combustion zone in the upper bed. Oyama et al. [7] indicated that gas fuel

injection had a potential to improve sintering energy efficiency. Wu et al. [8] developed a rapid visual method for gas injection that could provide technical support for gas fuel sintering technology. Wang et al. [9] reported a flue gas recycling sintering technology and studied the effects of flue gas recycling on temperature distribution in the sintering bed. Ni et al. [10] studied coke oven gas (COG) injection technology on a sintering bed surface. The results of their study indicated that the temperature evolution curves of the sintering bed were different from those of CS. Gao et al. [4] demonstrated that natural gas (NG) injection in a sintering bed indeed improved the sinter strength in the upper layer. Zhou et al. [11] found that injection of a hydrogen-bearing gas during sintering significantly improves the heat distribution in the sintering bed. An iron ore sintering process using gaseous fuels has been confirmed to optimize the heat distribution in the sintering bed. However, the use of gaseous fuels to replace solid fuels, such as coal/coke breeze, is uneconomical, and this technology requires gas injection equipment that is costly to design and build. Moreover, gaseous fuel injection has a risk of explosion because of the lower ignition temperature of gas fuels compared with that of solid fuels. In this context, rare industrial application of gaseous fuel injection sintering technology has been conducted at large-scale and low-cost. Therefore, further studies on how to improve the uneven heat distribution in CS are necessary.

A double-layer segregation distribution of the solid fuel in the sintering process was proposed. Sumitomo Metals Corporation in Japan [12] conducted studies on the double-layer segregation distribution of solid fuel and designed a two-stage ignition sintering process. This technology addressed the uneven fuel distribution between the upper and bottom bed layers, in which the bottom layer may not combust well and even flameout. Petrushev et al. [13] also studied the regular distribution and segregation distribution of fuel in sintering experiments. The findings of their investigation demonstrated that the temperatures in the upper and bottom layers of the sintering bed differed between the two sintering methods. Anshan Iron and Steel Group in China [14] conducted sinter pot tests to study the double-layer segregation distribution of solid fuel in the sintering process and indicated that oxygen-enriched operation should be applied when the sintering bed height is more than 1000 mm. Xu [15] reported that the sintering bed height of the upper and bottom beds affected the sintering quality, and the segregation distribution degree of the fuel was a key parameter in this technology. In previous studies, no one has assessed the detailed effect of the fuel segregation distribution dosage on the sintering process and sinter quality variation between the CS and fuel segregation distribution sintering (FSDS) processes under similar fuel consumption conditions. In addition, the appropriate technology parameters of FSDS have rarely been studied and reported. Appropriate technology parameters, including the fuel distribution in the upper/bottom bed layers and the heights of the upper/bottom bed layers, are significant in iron ore sintering. Therefore, the above-mentioned parameters and their effects on sinter quality should be investigated. Further studies on the FSDS technology are necessary to enhance sinter quality uniformity in the bed height direction.

Research methods for iron ore sintering generally include experimental research and numerical simulations. Experimental research is generally performed using sinter pot tests to simulate a local sintering process. Numerical simulations are conducted via CFD modelling, which could further enhance the understanding of the sintering process.

Regarding numerical simulation research, Young et al. [16] developed a model to investigate mass and heat transfer in the sintering layers. Vizureanu et al. [17] established a mathematical model of the nanofluid heat transfer to study the dynamics of the fluid/particle interface based on the fractal space–time theory, which provided empirical guidance for future research about this issue. Oyama et al. [18] established a model for the iron ore fines sintering process under an unsteady state. They focused on convective heat transfer, including coke combustion and water evaporation, in the sintering process. Ramos et al. [19] reported a numerical model that considers bed structural changes via the discrete element method. Yang et al. [20] also built a sintering process model that considers

multiple-phase reactions, such as water drying, limestone decomposition, coke combustion, and bed layer shrinkage. However, Yang's model does not consider the melting and solidification processes in the sintering bed. Castro et al. [5,21] also established a mathematical model for iron ore sintering, and they referred to most of the chemical reactions in the sintering process.

Previous mathematical models have mainly focused on conventional sintering processes or combustible gas-injection sintering processes. Only a few studies have investigated the FSDS process. In this study, a model was developed to study the FSDS and CS technologies contrastively. In addition, different thicknesses of the upper and bottom bed layers were employed to assess the FSDS technology and determine the appropriate technology parameters. Parameters such as the cooling rate, melt quantity index, amount of binding liquid phase, and solid-phase temperature evolution in the sintering bed were adopted to evaluate the FSDS technology. The aim of this study was to provide reliable guidance for achieving fuel segregation distribution sintering. It can help to solve the problem of insufficient heat in the upper part and excess heat in the lower part of the sintering bed existing in the conventional iron ore sintering process. Furthermore, the quality of the fired sinter can be therefore improved.

2. Mathematical Model

The iron ore sintering process is occurred at high temperature and complex physical and chemical changes with two-dimensional (2D) characteristics. The following simplification was made based on the multi-space medium model in the process of model establishment and heat transfer analysis.

- (1) Considering that the physical parameters of the gas phase and the solid phase have almost no change in the cross section of the material layer, the iron ore sintering process can be regarded as a 2D unsteady process.
- (2) Due to the small particle size and the larger thermal conductivity of the particle, the temperature inside and outside the particle is regarded as uniform, and the heat transfer inside the particle is ignored.
- (3) The convective heat transfer is considered as a dominant. Therefore, the other heat transfer modes are ignored in our model.
- (4) The solid and gas in the material layer are treated as continuous mediums, and the material layer is considered as a uniform porous medium. The variation of the sinter layer geometry size, caused by the gas–solid phase reaction, is simplified into two parts of porosity and equivalent diameter of mixed particles.

2.1. Gas phase Control Equation

The gas phase control equations were used to determine the temperature, mass, velocity, and as flue gas components in the sintering bed.

(1) Continuity equation

$$\frac{\partial(\varepsilon\rho_g)}{\partial t} + \frac{\partial}{\partial x_j}(\varepsilon\rho_g U_{i,g}) = M_s + M_g, \quad (1)$$

(2) Momentum equation

$$\frac{\partial}{\partial t}(\varepsilon\rho_g U_{i,j}) + \frac{\partial}{\partial x_j}(\varepsilon\rho_g U_{i,g} U_{j,g}) = \frac{\partial}{\partial x_j} \left(\mu_g \frac{\partial U_{i,g}}{\partial x_j} \right) - \frac{\partial P}{\partial x_j} - I_j, \quad (2)$$

For porous media, the resistance source term includes two parts: viscosity resistance and inertia resistance.

$$I_j = \frac{150\mu_g(1-\varepsilon)^2}{d_p^2\varepsilon^3} U_{i,g} + \frac{1.75\rho_g(1-\varepsilon)}{d_p\varepsilon^3} U_{i,g} U_{j,g}, \quad (3)$$

(3) Energy equation

The energy equation was used to determine the heat transfer in the sintering bed, as described in Equation (4).

$$\frac{\partial}{\partial t}(\varepsilon\rho_g C_{p,g} T_g) + \frac{\partial}{\partial x_j}(\varepsilon\rho_g C_{p,g} U_{i,g} T_g) = \frac{\partial}{\partial x_j} \left(\lambda_{g,eff} \frac{\partial T_g}{\partial x_j} \right) + Q_{conv} + H_s + Q_{sg}, \quad (4)$$

(4) Component transport equation

The component transport equation described in Equation (5) was used to determine the mass fractions of gases, such as O₂, H₂O, CO, CO₂, and N₂.

$$\frac{\partial(\varepsilon\rho_g X_{i,g})}{\partial t} + \frac{\partial}{\partial x_j}(\varepsilon\rho_g U_{i,g} X_{i,g}) = \frac{\partial}{\partial x_j} \left(\rho_g D_{i,m} \frac{\partial X_{i,g}}{\partial x_j} \right) + M_{i,g} + M_{i,s}, \quad (5)$$

2.2. Solid Phase Control Equation

(1) Continuity equation

$$\frac{\partial(1-\varepsilon)\rho_s}{\partial t} = -M_{s,r} \quad (6)$$

(2) Energy equation

The energy equation for the solid phase is given in Equation (7).

$$\frac{\partial((1-\varepsilon)\rho_s C_{p,s} T_s)}{\partial t} = \frac{\partial}{\partial x_j} \left(\lambda_{s,eff} \frac{\partial T_s}{\partial x_j} \right) - Q_{conv} - H_s + Q_{ss}, \quad (7)$$

(3) Component transport equation

$$\frac{\partial((1-\varepsilon)\rho_s X_{i,s})}{\partial t} = -M_{i,s,r} \quad (8)$$

2.3. Sub Models

Sub models can influence the accuracy of the overall model. In this study, the sub models include models for coke combustion, gas phase combustion, carbonate decomposition, and volume variations of the bed structure.

2.3.1. Model for Coke Gasification and Combustion

Coke gasification and combustion are important reactions in the sintering process. These reactions were described based on the unreacted core model. The details were provided in our previous study [4]. The coke combustion rate (R_{com}) is given by Equation (9).

$$C + O_2 = CO_2, \Delta H = -3.936 \times 10^5 \text{ J/mol},$$

$$R_{com} = \frac{CO_2 4\pi r_0^2 n}{\frac{1}{k_f} + \frac{1}{k_c} \left(\frac{r_0}{r_c}\right)^2 + \frac{r_0(r_0-r_c)}{D_e r_c}} \quad (9)$$

The coke gasification rate (R_{gas}) is described in Equation (10).

$$C + CO_2 = 2CO, \Delta H = 1.78 \times 10^5 \text{ J/mol},$$

$$R_{gas} = \frac{C_{CO_2} 4\pi r_0^2 n}{\frac{1}{k_{f1}} + \frac{3}{k_{c1} E_{f1} r_c \rho_c}} \quad (10)$$

2.3.2. Model for Water Evaporation and Condensation

Water evaporation and condensation significantly influence the permeability of the sintering bed. Moreover, they consume more than 15% of the total sintering energy. The water evaporation rate (R_{eva}) is described as follows, and the details were described in our previous paper [4]:

$$\begin{aligned} \text{H}_2\text{O}_{(l)} &= \text{H}_2\text{O}_{(g)} \quad \Delta H = 4.06 \times 10^4 \text{ J/mol}, \\ R_{\text{eva}} &= \varphi \frac{\beta_{\text{H}_2\text{O}} S}{R_g T_g} (P_{\text{H}_2\text{O}}^* - P_{\text{H}_2\text{O}}) \end{aligned} \quad (11)$$

2.3.3. Model for Solidification and Melting

Solidification and melting are controlled by the removal and addition of heat, respectively. The solidus temperature of the melting phase (T_1) is regarded as a variable, along with the solid composition, as described in Equation (12) [9]. The liquidus temperature of the melting phase (T_2) was set to 1673 K, based on a previous study [9]. Solidification was considered a reverse process of melting.

$$T_1 = 1280 + 21.22Al_2O_3 + 3.35SiO_2 - 1.8flux, \quad (12)$$

where SiO_2 , Al_2O_3 , and $flux$ indicate the corresponding mass contents in raw mix. The melting fraction is defined in Equation (13) [10] as follows:

$$M_f = \min\left(\frac{T_s - T_1}{T_2 - T_1}, 1\right), T_s > T_1, \quad (13)$$

2.3.4. Model for Structure Changes of the Sintering Bed

The structural variations of the bed, which are caused by gas–solid reactions, such as coke combustion and gasification, were also considered in our model. The variations considered were: (1) sintering bed porosity and (2) equivalent diameter of the granulated materials [22].

(1) Equation for the changes in bed porosity

Bed porosity has a significant effect on gas and temperature distributions. The porosity of the sintering bed is described in Equation (14) [22].

$$\varepsilon = \varepsilon_0 + \frac{(\phi_0 - \phi)(1 - \varepsilon_0)}{\phi_0 - 0.07} - \frac{(1 - \varepsilon_0)\lambda}{1 - \lambda} + \frac{4\pi n_c (r_0^3 - r_t^3)}{3}, \quad (14)$$

Shape coefficient:

$$\phi = \phi_1 - \frac{(\phi_1 - \phi_0)(T_s - T_1)}{T_{\text{max}} - T_1}, \quad (15)$$

Shrinkage rate of material layer:

$$\lambda = \frac{(\phi_0 - \phi)\lambda_{\text{max}}}{T_s - T_1}, \quad (16)$$

Instantaneous radius of coke combustion process:

$$r_t = r_0 \cdot \left(\frac{m_t}{m_0}\right)^{\frac{1}{3}}, \quad (17)$$

(2) Equation for the changes in the equivalent diameter of mixed particles

The changes in the equivalent diameter of mixed particles were determined in a previous paper [9]. This can be described by Equation (18).

$$d_p = d_{p0} + \frac{(T_s - T_1)(d_{p1} - d_{p0})}{T_{\text{max}}}, \quad (18)$$

2.3.5. Other Models

Other reaction models including dolomite decomposition [23,24], limestone decomposition [25–28], hematite reduction, magnetite oxidation, and combined water release from $\text{Ca}(\text{OH})_2$ [9] were determined based on previous studies. In addition, the CO combustion reactions in the sintering process were calculated, as reported by Gao et al. [4].

2.4. Model Solution and Boundary Conditions

(1) Model solution

The control equations were solved using a user-defined function (UDF) and Fluent software. Variations in energy and mass were considered as the source terms of the control equations. The SIMPLE algorithm was adopted to solve the control equations. Since each variable in the material layer changed greatly with time in the sintering process, the time term of the governing equation was retained and solved by two-dimensional unsteady state. The turbulence model was adopted in this work. The vorticity dissipation model of component transport and the chemical reaction in the sintering process were compiled by UDF and added into the governing equation in form of the heat source terms. When the energy equation error is less than 10^{-6} and the other equations error is less than 10^{-3} , respectively, the model solution process is regarded as convergence. The solution flow is illustrated in Figure 4.

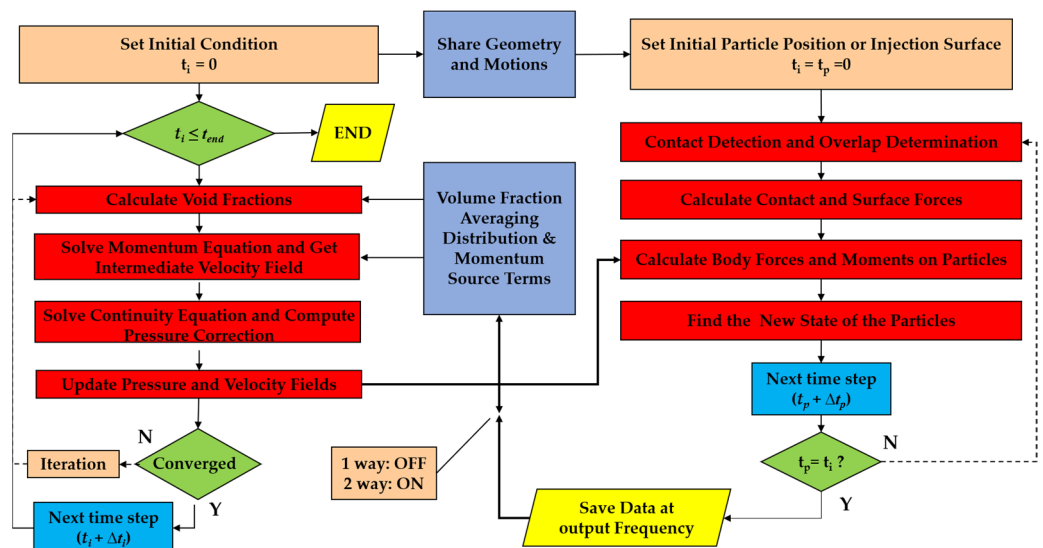


Figure 4. Flow chart for the model solution.

(2) Boundary conditions

The model boundary conditions include the ignition temperature, ignition duration time, moisture content of the mixed materials, initial gas temperature, and initial solid temperature. The details are presented in Table 1.

Table 1. Boundary conditions.

Average particle diameter: 3 mm diameter (m) 0.0030	Bed height: 600 mm
Ignition duration time: 120 s	Ignition temperature: 1373 K
Negative pressure during ignition: −10 kPa	Negative pressure after ignition: −15.0 kPa
Moisture content: 6.0%	Initial temperature of solid: 298 K
Bed porosity: 0.26	Initial temperature of gas: 298 K
Flow rate of gas during ignition: 4 m/s	Flow rate of gas after ignition: 0.4 m/s

The physical model of simplified sinter section was established, the calculation domain of sinter layer was determined, and a two-dimensional (2D) physical model of 300 mm width and 600 mm height was established. The model contains 8400 quadrilateral cells, 70 2D velocity inlet faces, 70 2D pressure outlet faces, 240 2D wall faces, 16,610 2D interior faces, and 8591 nodes. Figure 5 shows a sintering model calculation grid. The pressure outlet and velocity inlet were used here. The heat loss through the sintering machine wall was obtained based on other studies [10,26].

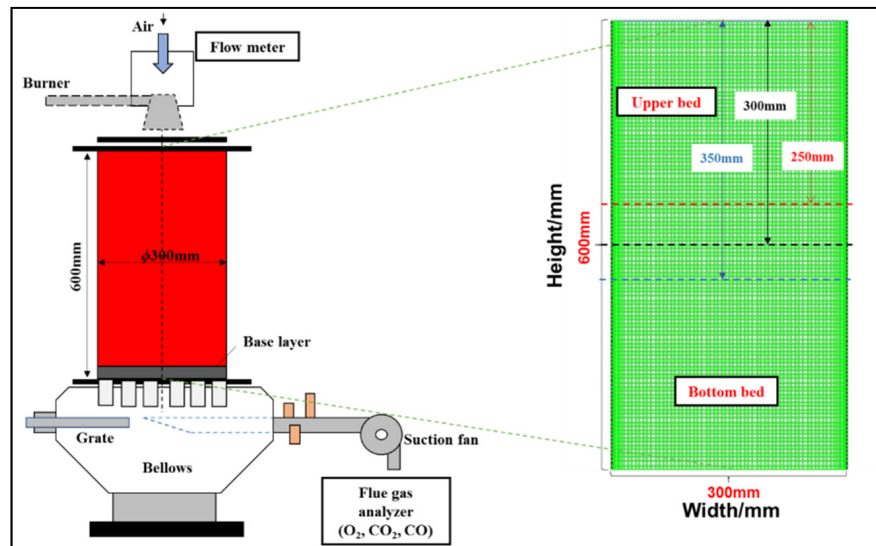


Figure 5. Schematic of the model calculation grid.

2.5. Sinter Pot Experiments

Sinter pot experiments were conducted to test the proposed model. A schematic of the experimental setup is shown in Figure 6. Thermo-couples (T.C) were inserted into the sintering bed to examine the temperature distribution along the y direction with a bed height of 600 mm, which was divided into two parts: upper bed layer (heights: 300, 250, and 350 mm) and bottom bed layer (heights: 300, 350, and 250 mm).

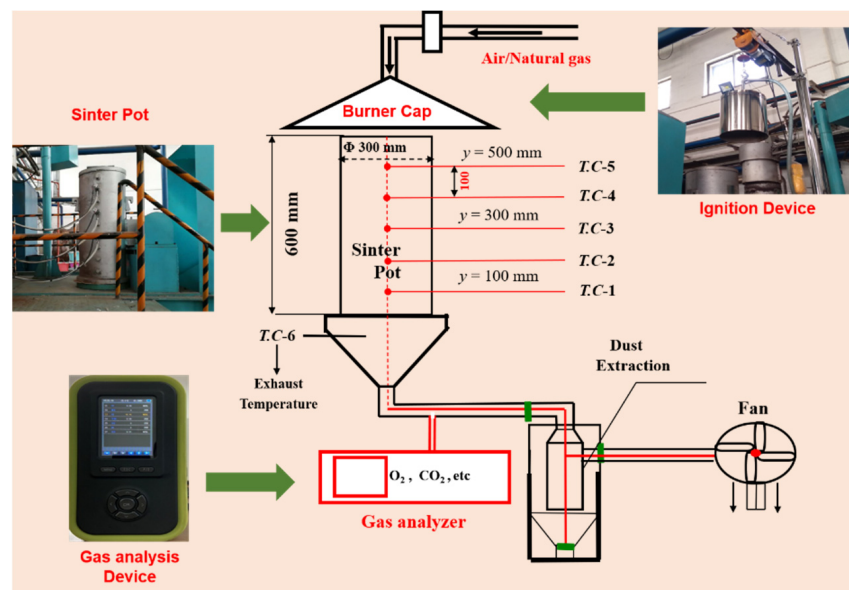


Figure 6. Schematic of the sintering experiments.

The experimental parameters are listed in Table 1. The compositions of the raw materials and their corresponding proportions are presented in Table 2.

Table 2. Compositions and proportions of the raw materials.

Raw Materials	Chemical Composition						Proportion/%
	TFe	w (CaO)	w (SiO ₂)	w (MgO)	w (Al ₂ O ₃)	LOI	
Iron ore fines	57.35	0.56	5.85	0.44	1.30	0.19	80.12
Coke breeze	0.02	2.92	34.02	0.79	24.91	85.44	4.50
Quick lime	<0.10	84.99	2.56	0.77	0.00	10.31	8.66
Dolomite	0.29	29.88	0.99	22.51	0.31	45.22	2.86
Limestone	0.06	53.22	1.98	0.87	0.65	43.01	2.51
Serpentine	<0.10	2.10	39.58	39.90	0.83	14.98	1.35

The sinter pot experiments were carried out as follows:

- (1) The mixing machine was used to mix the raw materials (including iron ore fine, fluxes, and fuel), and then granulate them to the spheroidal particles.
- (2) The granulated spheroidal particles with different carbon content were placed into the sintered pot successively. The detailed parameters, such as bed height and carbon content, are listed in Table 3.
- (3) The sinter pot was ignited and sintering process was conducted. The experimental data were auto-recorded by a computer. After the experiments, the data were collected for the further analysis.

Table 3. Experiment and calculation schemes.

Cases	Bed Height/mm		Carbon Content/%		Average Carbon Content/%
	Upper Bed	Bottom Bed	Upper Bed	Bottom Bed	
Base case	300	300	4	4.00	4
Case I	300	300	5	3.00	4
Case II	250	350	5	3.29	4
Case III	350	250	5	2.60	4

2.6. Calculation Schemes

The detailed calculation schemes are also presented in Table 3. What needs illustration is that all calculation cases were maintained at the same energy consumption with an average carbon content of 4.0% in mixed sintering materials.

The base case was a CS process with an even fuel distribution in the sintering bed. Case I was an FSDS process with high and low fuel dosages in the upper and bottom beds, respectively. Both the upper and bottom bed heights of Case I were set to 300 mm, and the carbon contents in the upper and bottom bed were maintained at 5.0% and 3.0%, respectively. Case II was an FSDS process with upper and bottom bed heights of 250 and of 350 mm, respectively, and the carbon contents in the upper and bottom bed layers were maintained at 5.0% and 3.29%, respectively. Case III was an FSDS process with upper and bottom bed heights of 350 and of 250 mm, respectively, and the carbon contents in the upper and bottom bed layers were maintained at 5.0% and 2.6%, respectively. The base case and Case I were chosen to contrastively study the CS and FSDS technologies. Cases I, II, and III were selected for the determination of the effect of bed heights of the upper and bottom layers on the sintering process.

2.7. Evaluation Indexes for Sinter Quality

(1) Cooling rate (CR) and melt quantity index (MQI)

Figure 7 presents the temperature variation at a certain location in the sintering bed over time. In addition, t_1 , t_2 , and t_{\max} represent the times when the raw materials begin to melt, solidify, and reach the maximum temperature (T_{\max}), respectively. The horizontal line represents the melting point of the sintered material. Based on a previous study [9], $T_1 = 1300$ K. Some important indexes, such as the maximum temperature (T_{\max}), residence time in the melt zone ($t_2 - t_1$), and cooling time ($t_2 - t_{\max}$), can be obtained from this curve. The cooling rate is given by Equation (19), which was applied to study the cooling of iron ore fines during sintering. When CR was larger, the residence time in the high-temperature zone was shorter, which could weaken the sinter strength. In addition, MQI, as described in Equation (20), was used to describe the melt quantity during the sintering process [29].

$$\text{CR} = \frac{T_{\max} - T_1}{t_2 - t_{\max}}, \quad (19)$$

$$\text{MQI} = \int_{t_1}^{t_2} (T_s - T_1) dt, \quad (20)$$

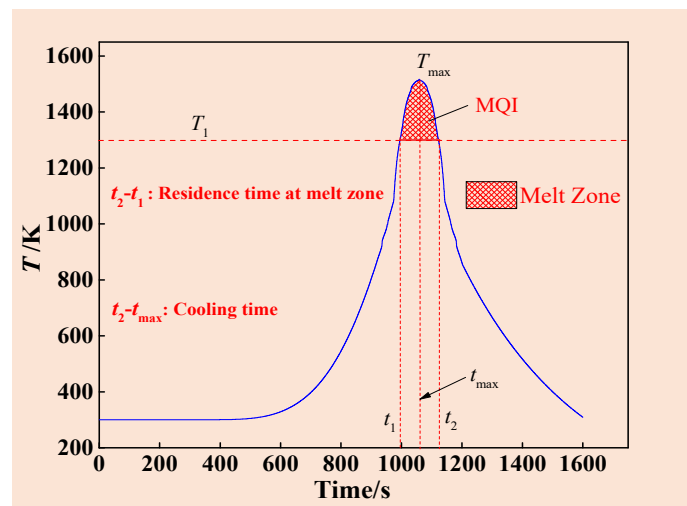


Figure 7. Temperature curve of the solid phase sintering bed.

(2) Melt fraction (Mf)

The Mf was defined to describe the amount of the binding phase in the sintering process, as described in Equation (21).

$$\text{Mf} = \begin{cases} 1, & (T_s > T_2) \\ \frac{T_s - T_1}{T_2 - T_1}, & (T_1 \leq T_s \leq T_2) \\ 0, & (T_s < T_1) \end{cases}, \quad (21)$$

T_1 was set to 1300 K based on a previous study [9]. Mf was used to determine the sinter yield. In fact, an Mf value that is too large or too small will cause over-melting or under-melting, respectively, during the sintering process. Nath et al. [30] stated that a sinter was under-melted when $\text{Mf} < 0.15$, and over-melted when $\text{Mf} > 0.45$; thus, a sinter with an Mf between 0.15 and 0.45 was regarded as a qualified product. This evaluation method was also adopted in this study.

3. Results and Discussion

3.1. Validation of Model Accuracy

The temperature variation in the solid phase of the bed and composition of the exhaust gas obtained from the model calculations and sintering experiments are shown in Figure 8. The results calculated using our model were consistent with those obtained from the sintering tests. For instance, the error of temperature evolution between the experimental and the calculation results was less than 5%, indicating that the model demonstrated high accuracy.

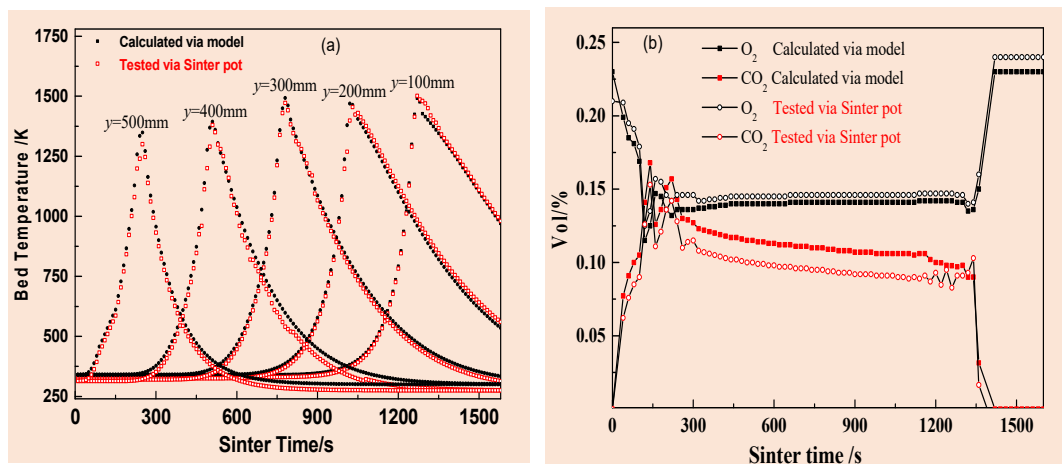


Figure 8. Results obtained from the model calculation and experimental tests. (a) temperature evolution at different bed heights; (b) exhaust gas composition.

3.2. Comparison of the CS and FSDS Technologies with the Same Heights of the Upper and Bottom Bed

The temperature fields in the sintering bed were simulated to compare the CS and FSDS technologies. The detailed results of temperature distribution along with sintering time at vertical centerline of the material layer for the base case (CS) and case I (FSDS) are shown in Figure 9.

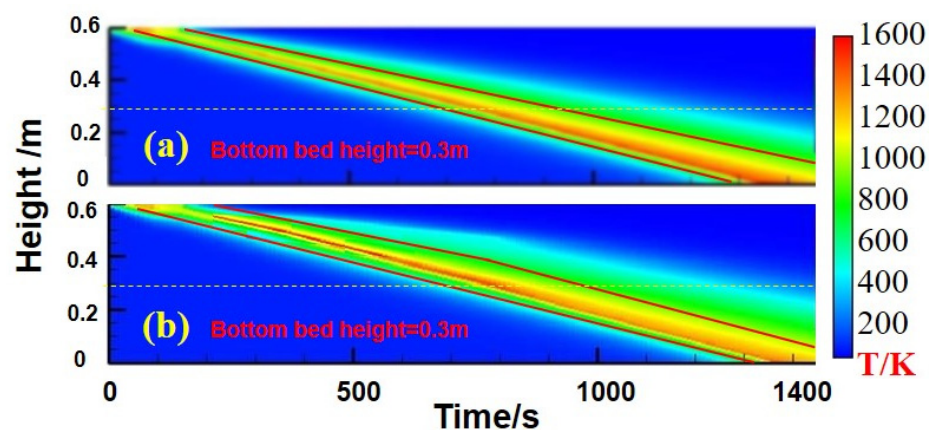


Figure 9. Temperature field in the sintering bed. (a) base case; (b) case I.

As shown in Figure 9a, iron ore sintering was conducted together with exothermic fuel combustion. The temperature of the combustion zone gradually increased from the upper to the bottom of the sintering bed, owing to the heat shift from the upper to the bottom of the bed. In addition, the combustion zone widened when fuel combustion propagated downward. The accumulation of heat occurred in the bottom of the sintering bed, indicating that the lack of heat in the upper bed and the excess of heat in the bottom

bed occurred in the CS technology, which resulted in a difference in the sinter quality of the upper and bottom beds. In Figure 9b, the high-temperature area and maximum temperature in the sintering bed increased in the upper layer bed and decreased in the bottom layer bed when the FSDS technology was implemented, indicating that the heat was distributed more uniformly. This result was in accord with the conclusion reported by Feoktistov et al. [12].

(1) Thickness of high-temperature zone

The temperature sections of the sintering bed at 300, 500, 700, 900, and 1100 s are shown in Figure 10.

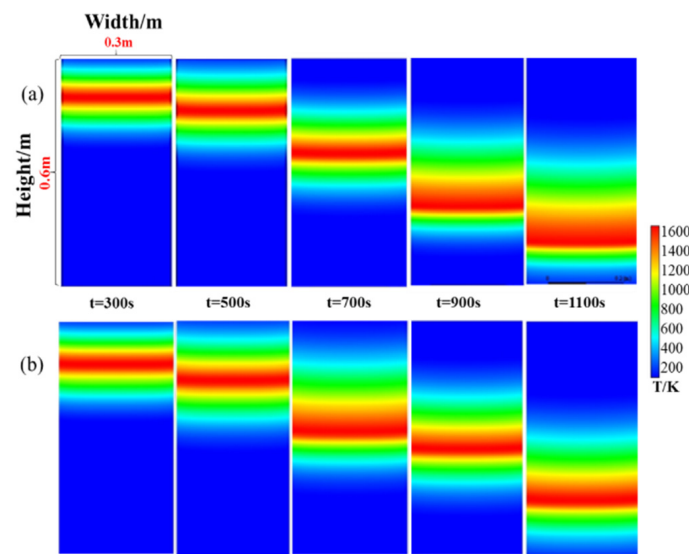


Figure 10. Temperature distributions at various times. (a) base case; (b) case I.

Base case and Case I were chosen to contrastively study the two sintering technologies: CS (Figure 10a) and FSDS (Figure 10b). As shown in Figure 10, compared with the CS technology (base case), the thicknesses of the high-temperature zone using the FSDS technology (case I) at 300, 500, and 700 s increased gradually as the sintering positions were located at the upper sintering bed. This confirmed that the FSDS technology could extend the maintenance time of the high-temperature zone in the upper sintering bed and improve the sinter quality in the upper layer of the bed. Moreover, at 900 and 1100 s, the thickness of the high-temperature zone using the FSDS technology gradually decreased as the sintering positions were located at the bottom bed. This indicates that excessive heat could be avoided. These variations are caused by the low fuel dosage of the FSDS technology in the lower layer and high fuel dosage in the upper layer of the sintering bed.

(2) Sintering bed temperature at different heights

The solid-phase temperature curves of the sintering bed are regarded as a significant factor for understanding the sintering process, which influence the yield and quality of the fired sinter. Consequently, a quantitative investigation of the solid-phase temperature evolution process is necessary. The temperature distribution curves for the CS and FSDS technologies are shown in Figure 11. In contrast to the base case (CS technology), the peak temperatures of the upper bed ($y = 0.5, 0.4,$ and 0.3 m) for case I (FSDS technology) gradually increased, and those in the bottom bed ($y = 0.2$ and 0.1 m) tended to decrease. Considering the position $y = 0.4$ m as an example, the temperature difference between the CS and FSDS technologies nearly reached 300 K. In addition, the high-temperature zone residence time for the upper bed increased correspondingly, which was confirmed by the broadened curves of the temperature distribution. These changes can help in addressing the heat deficiency in the upper bed of the CS technology.

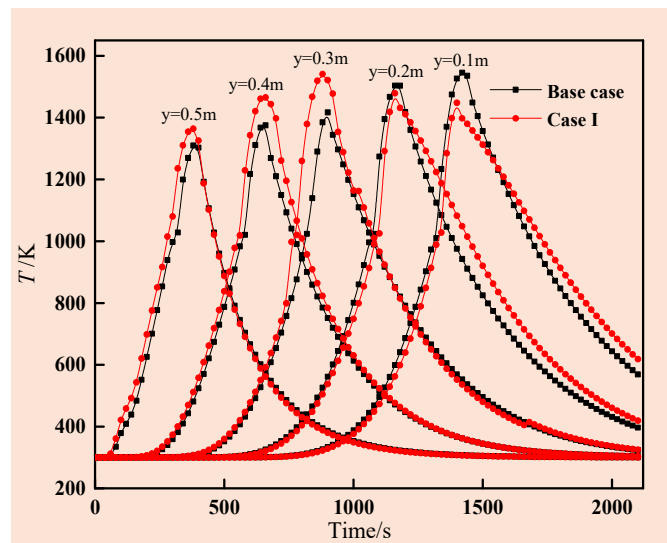


Figure 11. Temperature evolution curves of CS (Base case) and FSDS (Case I).

(3) Cooling rate and melt quantity index

Ni et al. [10], Loo et al. [31], Zhang [32], and Liu et al. [33] proved that the MQI is directly proportional to the tumbler strength of a fired sinter. Based on the temperature distribution shown in Figure 11, the corresponding CR and MQI values at different bed heights were obtained, as shown in Figure 12. From Figure 12, it was concluded that MQI decreased with increasing bed height. Because the MQI represented the degree of heat accumulation in the sintering bed, a smaller MQI could cause the temperature to drop more quickly, leading to a gradual increase in CR. In fact, CR appears to be inversely proportional to MQI. Therefore, CR and MQI are generally adopted to assess sinter quality. As shown in Figure 12, the sintering bed was divided into the upper layer and bottom layer bounded from the height of $y = 0.3$ m. Compared with the CS technology (base case), the MQI of the upper layer ($y = 0.5, 0.4,$ and 0.3 m) for the FSDS technology (case I) gradually increased, and that in the bottom layer ($y = 0.2$ and 0.1 m) tended to decrease. The CR of the FSDS technology was lower than that of the CS technology. This difference was caused by the low fuel dosage in the lower layer and high fuel dosage in the upper layer for the FSDS technology, which provided sufficient heat in the upper layer and prevented excessive heat in the lower layer.

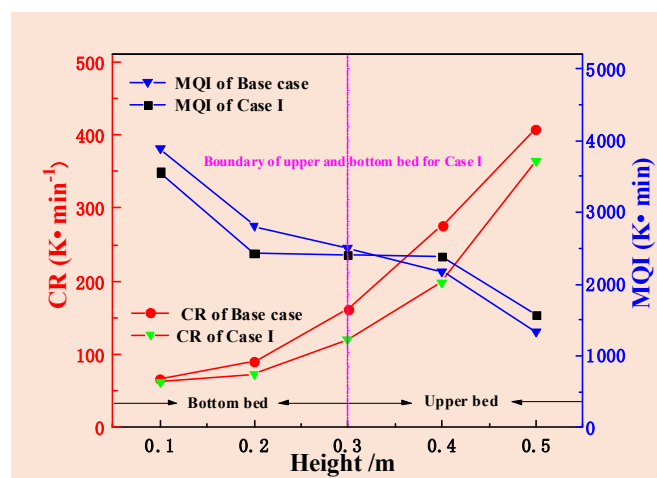


Figure 12. Comparison of CR and MQI for FSDS and CS technology.

Parameters such as maximum temperature (T_{\max}), residence time of melt zone, and MQI and CR at bed heights of 0.4 m (upper bed) and 0.1 m (bottom bed) for the CS and FSDS technologies are presented in Table 4.

Table 4. Some parameters from temperature curves for the CS and FSDS technologies.

Cases	T_{\max}/K		Residence Time of Melting Zone/s		MQI/(K·min)		CR/(K·min ⁻¹)	
	$y = 0.4 \text{ m}$	$y = 0.1 \text{ m}$	$y = 0.4 \text{ m}$	$y = 0.1 \text{ m}$	$y = 0.4 \text{ m}$	$y = 0.1 \text{ m}$	$y = 0.4 \text{ m}$	$y = 0.1 \text{ m}$
Base case	1390	1540	59	140	2178	3895	360	67
Case I	1466	1461	122	155	2387	3500	199	63

The following conclusions can be drawn from Table 4. (1) The T_{\max} at the upper bed ($y = 0.4 \text{ m}$) and bottom bed ($y = 0.1 \text{ m}$) were 1390 and 1540 K, respectively, for the base case, and the temperature difference between the T_{\max} for the upper and bottom layer was 150 K. For the FSDS technology (case I), the T_{\max} of the upper bed quickly increased to 1466 K and that of the bottom bed decreased to 1461 K; the corresponding temperature difference of the T_{\max} was 5 K, indicating that the sintering bed temperature was more even when using the FSDS technology. (2) Compared with the CS technology (base case), the residence times of the melting zone under case I increased in the upper bed, which indicates that the reactions that occurred during sintering were adequate; more binding liquid phase were generated, which enhanced the sinter quality. (3) Compared with the CS technology (base case), the MQI in Case I increased in the upper bed and decreased in the bottom bed. This was due to a longer high-temperature zone, which increased the fuel dosage in the upper bed. The enhanced MQI indicates that the strength of the sinter in the upper bed was improved. In addition, the CR values for the upper and lower layers decreased. For instance, the CR quickly decreased from 360 to 199 K·min⁻¹. The decreasing CR signifies that the rapid cooling, which is detrimental to the quality of the sinter, was restrained, thereby improving the component uniformity of the fired sinter.

(4) Melting fraction (Mf)

The iron ore sintering process aims to achieve fine ore consolidation via cohesive action of the binding phase to attain a high-strength sinter. Thus, the amount of the binding phase generated between the fluxes and iron ore under high-temperature conditions is considered as an important parameter. In general, calcium ferrite minerals formed from the reaction between CaO-bearing fluxes and iron oxides are considered to be the main binding phase. Hence, the binding phase amount was investigated in this study. The Mf distributions for the base case (CS) and Case I (FSDS) in the sintering bed are shown in Figure 13. As shown in Figure 13a, the Mf increased gradually in the base case when the sintering process propagated from top to bottom and reached a maximum value at the bottom layer of sintering bed. However, compared with the base case (CS), the Mf in case I appeared to be more adequate in the upper layer and apparently decreased in the bottom layer. This result confirmed that the FSDS technology not only increased the amount of binding phase in the upper layer of sintering bed, but also reduced that of the bottom layer. Therefore, the FSDS technology could make sinter quality more uniform in the entire sintering bed.

The detailed Mf values at different bed heights for the two technologies are shown in Figure 14. As shown in Figure 14, there was a sudden decline in the Mf values for both the Base case and case I during the initial sintering stage. This was due to the quantity of room air that entered the sintering bed during ignition, which caused a sharp temperature drop. The maximum Mf appeared at the bottom bed for the base case and at a bed height of 0.3 m for case I.

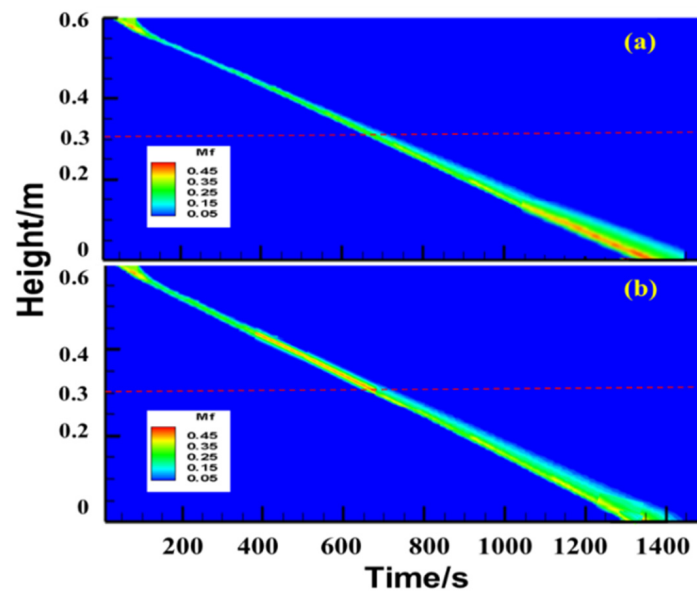


Figure 13. Melting fractions for the CS and FSDS technologies: (a) base case; (b) case I.

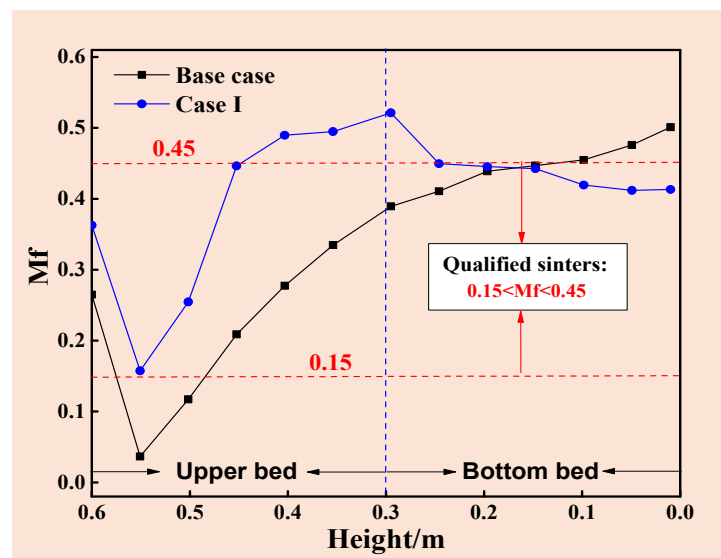


Figure 14. Mfs for CS (base case) and FSDS (case I) in sintering bed.

Some of the parameters obtained from Figure 14. are listed in Table 5. In our work, the sinter with an Mf value between 0.15 and 0.45 was regarded as the acceptable product. Table 5 showed that the maximum Mfs (Mf_{max}) of the two technologies were similar. Compared with the base case, the over-melted sinter ($Mf > 0.45\%$) increased from 22.75% to 33.33%, and the under-melted sinter ($Mf < 0.15\%$) disappeared when the FSDS technology (case I) was used. This caused the amount of the qualified sinter to increase from 61.82% to 66.67%. The sinter yields obtained from the sintering experiments for the base case and case I were 60.7% and 65.8, respectively, indicating that the calculation results of the model were well consistent with the test results of the sintering experiments.

In summary, the FSDS technology can positively affect iron ore fines sintering. The high-temperature zone residence time in the upper bed can be extended, and the heat can be used well in the upper bed. Moreover, problems existing in the CS process, such as excess heat accumulation in the bottom bed and lack of heat distribution in the upper bed, can be restrained. Therefore, the distribution of combustion heat is more even along the bed height direction. This conclusion is verified by the changes in Mf, as shown in Table 5.

In addition, the fired sinter yield was improved after adopting the FSDS technology, which was due to the uniform heat distribution in the bed height direction.

Table 5. Analysis of the M_f for the two technologies.

Cases	$M_{f_{max}}$	Under-Melted/% ($M_f < 0.15$)	Over-Melted/% ($M_f > 0.45$)	Qualified Sinter/% ($0.15 < M_f < 0.45$)	Qualified Sinter/% (Laboratory Trials)
Base case	0.504	15.43	22.75	61.82	60.7
Case I	0.521	0	33.33	66.67	65.8

3.3. Influence of the Different Heights of the Upper and Bottom Layers of the Sintering Bed on FSDS Technology

In this study, the FSDS technology was used and we studied the difference between the CS and FSDS technologies with same heights of the upper and lower bed layers, as discussed in Section 3.2. In fact, the heights of the upper and lower bed layers together also positively or negatively influence the FSDS technology. Therefore, different thicknesses of the upper and lower bed layers were designed and discussed, to comprehensively assess the FSDS technology and determine the appropriate technology parameters. Cases I, II, and III with upper bed heights of 300, 250, and 350 mm, respectively, were designed to study the influence of the upper and bottom bed heights on both the fired sinter quality and iron ore sintering process.

The temperature fields were studied. The detailed results of temperature distribution along with sintering time at vertical centerline of the material layer for Cases I, II, and III are shown in Figure 15.

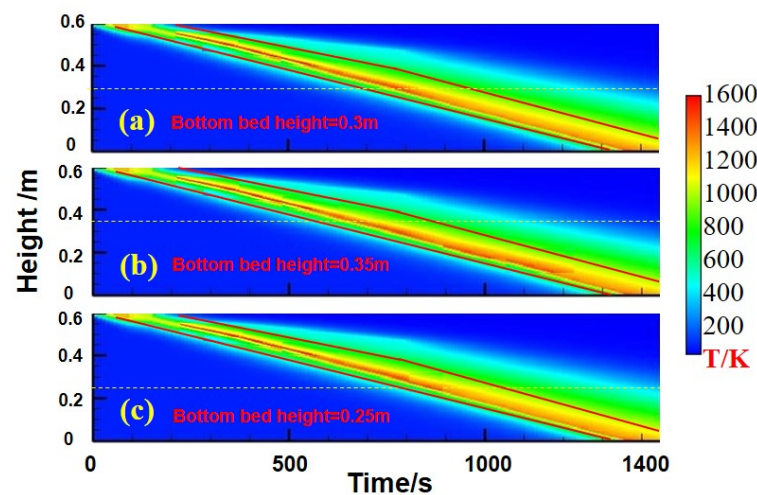


Figure 15. Temperature fields for FSDS technology with different bottom bed heights. (a) case I; (b) case II; (c) case III.

The following conclusions can be drawn from Figure 15. (1) The high-temperature zone area in the upper bed for case II was similar to that for case I (FSDS technology with similar upper and bottom bed heights) because the carbon content in the mixed sintering materials was maintained at 5.0%. (2) The high-temperature area in the bottom bed for case III (with a thicker upper bed and thinner bottom bed) was smaller than that for cases II and I because the carbon content for case III in the bottom bed was lower than those for cases II and I.

(1) Sintering bed temperature at different heights

The temperature distributions at different bed heights for cases I, II, and III are presented in Figure 16. The peak temperatures of the upper sintering bed ($y = 0.5$ and 0.4 m) for cases I, II, and III were consistent because the carbon content in these cases were 5.0%, as

shown in Table 3. The peak temperature at a bed height of $y = 0.3$ m for case II (upper bed height = 250 mm and bottom bed height = 350 mm) was lower than those for cases III and I because the location of $y = 0.3$ m for case II was in the bottom layer of the sintering bed with low carbon content. The peak temperature at a bed height of $y = 0.1$ m for case III (upper bed height = 350 mm and bottom bed height = 250 mm) decreased significantly compared to cases II and I, indicating that the heat at the bottom bed in case III decreased significantly. Therefore, the heat distribution was also unreasonable using the FSDS technology when the upper bed height was greater than that of the bottom bed.

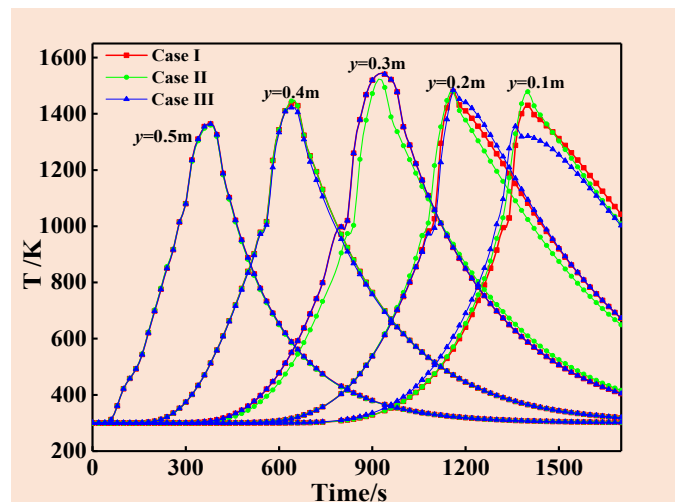


Figure 16. Temperature evolution curves of Case I, II and III.

(2) Cooling rate and melt quantity index

The MQI and CR for different heights of the upper and lower beds are shown in Figure 17. The heights of the upper and bottom beds mainly affected the MQI of the bottom bed. Compared with case I with equal upper and bottom bed heights, the MQI for the bottom bed shows a further decrease for case II, indicating that the issue on excessive heat was resolved. However, the MQI for case III at the position $y = 0.1$ m was too low, which weakened the sinter strength in the bottom bed. In addition, the heights of the upper and bottom beds had little influence on CR based on our calculation. In summary, case II, with a 250 mm upper bed height and 350 mm bottom bed height, showed better results based on the FSDS calculation.

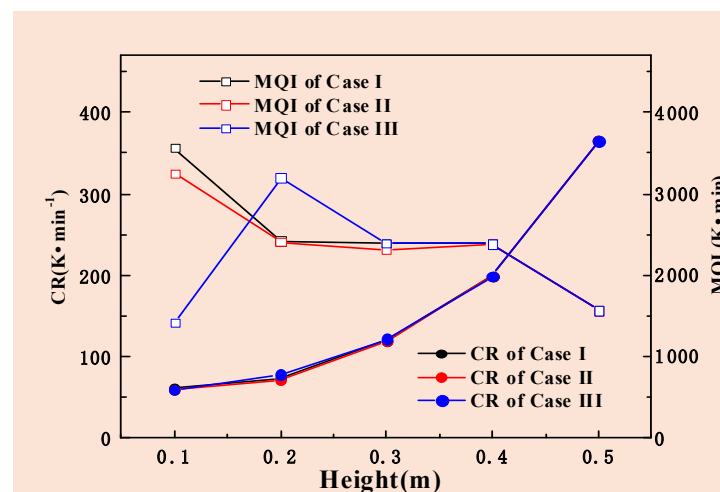


Figure 17. CR and MQI at different bed heights for case I, II and III.

The parameters such as the maximum temperature (T_{\max}), residence time of melt zone, MQI and CR at a bed height of 0.4 m (upper bed) and 0.1 m (lower bed) for the FSDS technology with different heights of upper and lower bed layers are presented in Table 6.

Table 6. Some parameters obtained from the temperature curves for cases I, II, and III.

Cases	T_{\max}/K		Residence Time of Melting Zone/s		MQI/(K·min)		CR/(K·min ⁻¹)	
	$y = 0.4m$	$y = 0.1m$	$y = 0.4m$	$y = 0.1m$	$y = 0.4m$	$y = 0.1m$	$y = 0.4$	$y = 0.1$
Case I	1466	1461	122	155	2387	3500	199	63
Case II	1466	1478	122	150	2387	3200	199	62
Case III	1466	1397	122	120	2387	1426	199	59

The following conclusions can be obtained from Table 6. (1) At an upper bed height of $y = 0.4$ m, the T_{\max} , residence time of melting zone, MQI, and CR for all the calculation cases had no differences because the carbon content in these cases were similar. (2) At a bottom bed height of $y = 0.1$ m, case II exhibited higher improvement owing to lower T_{\max} , shorter residence time of melting zone, and smaller MQI value. This was because the excess heat in the bottom bed was controlled. The corresponding parameters for case III at a position $y = 0.1$ m were unreasonably reflected in the excessively low T_{\max} owing to the excessively low fuel dosage in the bottom sintering bed. This change was also detrimental to the quality of the sinter.

(3) Melting fraction (Mf)

The Mf distributions for the FSDS technology with different thicknesses of the upper and bottom beds are shown in Figure 18. As shown in Figure 18, the maximum Mfs for cases I, II, and III were 0.521, 0.484, and 0.548, respectively. The position producing the maximum Mf for all cases was at the lower edge of the upper sintering bed. Some of the parameters obtained from Figure 18 are listed in Table 7. The under-melted sinter disappeared for all calculation cases. The quantity of over-melted sinter ($Mf > 0.45\%$) in case III was larger than those in cases I and II, which caused the amount of the qualified sinter in case III to be smaller than those in cases I and II, and even in base case (CS). Based on our study, compared with the CS (base case), the amount of the qualified sinter increased by 4.85% for case I and 21.66% for case II and decreased by 3.44% for case III. case II had a higher amount of qualified sinter (82.2%). Therefore, to obtain a higher amount of qualified sinter for the FSDS technology, the upper bed height should be smaller than the bottom bed height. In addition, the sinter yields obtained from the sintering experiments for cases I, II, and III were similar with those calculated by the model, indicating that the model calculations were accurate.

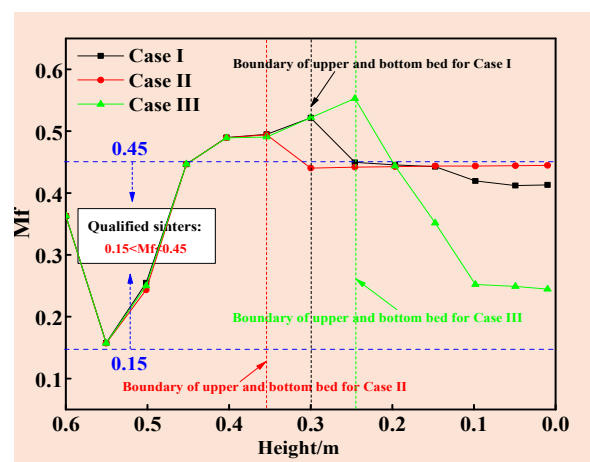


Figure 18. Mfs for cases I, II, and III at different bed heights.

Table 7. Analysis of Mf for case I, II and III.

Cases	Mf _{max}	Under-Melted/% (Mf < 0.15)	Over-Melted/% (Mf > 0.45)	Qualified Sinter/% (0.15 < Mf < 0.45)	Qualified Sinter/% (Laboratory Trials)
Case I	0.521	0	33.33	66.67	65.8
Case II	0.487	0	16.67	83.33	82.2
Case III	0.553	0	41.67	58.33	59.1

Based on the model results, the heights of the upper and bottom layers of the sintering bed can positively or negatively influence the FSDS technology. The heat distribution using the FSDS technology may be also uneven when the upper bed height was larger than the bottom bed height, as confirmed by the calculation for case III. The quantity of the qualified sinter for case III was the lowest among all the cases. Therefore, for better utilisation of the FSDS technology, the upper bed height should be smaller than the bottom bed height.

4. Evaluation of the FSDS Technology

Comparison between the CS process with even fuel distribution in the sintering bed and FSDS processes with high and low fuel dosages in the upper and lower bed layers, respectively, demonstrated that the FSDS technology can address the drawbacks of the CS technology, including the shortage of accumulated heat in the upper bed layer and excessive heat in the lower bed layer. In addition, the temperature distribution in the bed tended to be even and the accumulation of heat in the upper bed increased, which was confirmed by the increase in the MQI and decrease in the CR. Moreover, the residence time in the high-temperature zone in the upper bed increased correspondingly. The FSDS not only enhanced the amount of binding phase in the upper bed but also reduced it in the bottom bed, which made the quality of the fired sinter more uniform. Moreover, different thicknesses of the upper and lower bed layers positively or negatively affected the sinter quality. For instance, as the thicknesses of the upper and bottom beds were 250 and 350 mm, respectively, the sinter yield increased by 21.66% compared with CS, and this value decreased by 3.44% when the thicknesses of the upper and bottom beds were 350 and 250 mm, respectively. Therefore, reasonable heat distribution and uniform sinter quality can be realised by properly utilising the FSDS technology. The aim of this work was to provide reliable guidance for the application of the FSDS technology.

5. Conclusions

A calculation model was built to contrastively study the conventional iron ore sintering process with even fuel distribution in the sintering bed (CS) and the fuel segregation distribution sintering process with high fuel dosage in the upper layer and low fuel dosage in the bottom layer of sintering bed (FSDS). The main findings are summarized as follows:

- (1) The accuracy of the calculation model was verified by using the results of the sintering experiments. The error of temperature evolution between the experimental and the calculation results is less than 5%. The FSDS technology can address the drawbacks of the CS technology, including inadequate heat distribution in the upper sintering bed and excessive heat accumulation in the bottom sintering bed.
- (2) Some evaluation indices were adopted to assess the sinter quality, such as the MQI, CR, and Mf. Compared with the CS, the temperature evolution in the bed height direction for FSDS exhibited a more even heat distribution. The heat accumulation in the upper bed increased significantly, which demonstrated that the maximum temperature at $y = 0.4$ m (upper bed) increased by 76 K, the MQI increased from 2178 to 2387 K·min, and the CR decreased from 360 to 199 K·min⁻¹. In addition, the heat surplus issue in the lower bed was improved, which demonstrated the maximum temperature at $y = 0.1$ m (lower bed) reduced by 79 K and the MQI decreased from 3895 to 3500 K·min.

- (3) The different thicknesses of the upper and bottom beds affected the sintering process and sinter quality. For instance, when the thicknesses of the upper and bottom beds were 250 and 350 mm, respectively, the sinter yield increased by 21.66% compared with CS, and this value decreased by 3.44% when the thicknesses of the upper and bottom beds were 350 and 250 mm, respectively. Therefore, in order to effectively utilize the FSDS technology, the upper bed height should be designed to be smaller than the bottom bed height.

Author Contributions: Data curation, L.B.; methodology, Q.G.; investigation, P.Z.; supervision, X.J., H.Z. and F.S. All authors have read and agreed to the published version of the manuscript.

Funding: The work was supported financially by the National Natural Science Foundation of China (No.52074086, No.51974073, No.52074074, and No.52074072) and the Fundamental Research Funds for the Central Universities, China (N2225039).

Data Availability Statement: The data presented in this work are available from the corresponding author upon reasonable request.

Conflicts of Interest: The authors declare that they have no known competing financial interests or personal relationships that could have appeared to influence the work reported in this paper.

Nomenclature

$C_{p,g}$	specific heat of gases	$J \cdot kg^{-1} \cdot K^{-1}$
$C_{p,s}$	specific heat of solids	$J \cdot kg^{-1} \cdot K^{-1}$
C_{O_2}	concentration of O_2	$mol \cdot m^{-2}$
C_{CO_2}	concentration of CO_2	$mol \cdot m^{-2}$
D_e	mass diffusion coefficient of the gas phases	$m \cdot s^{-1}$
$D_{i,m}$	effective diffusion coefficient	–
d_p	equivalent diameter of the mixture particle	m
d_{p0}	initial particle equivalent diameter	m
d_{p1}	equivalent diameter of solidified particles	m
E_{f1}	effectiveness factor of coke and carbon dioxide	–
H_s	enthalpy of newly formed gas in gas-solid heterogeneous reaction	–
I_j	momentum source term in the x, y and z directions	$Ns \cdot m^{-2}$
k_c	coke combustion reaction rate constant	$m \cdot s^{-1}$
k_{c1}	gasification reaction rate constant	$m^3 \cdot kg^{-1} \cdot s^{-1}$
k_f	mass transfer coefficient of the gas boundary layer	$m \cdot s^{-1}$
k_{f1}	mass transfer coefficient of the gas boundary layer	$m \cdot s^{-1}$
M_s	mass of gas produced by gas-solid reaction	$kg \cdot m^{-3} \cdot s^{-1}$
M_g	mass of gas produced by homogeneous reaction of gases	$kg \cdot m^{-3} \cdot s^{-1}$
$M_{i,s}$	mass of gas components produced by gas-solid reaction	$kg \cdot m^{-3} \cdot s^{-1}$
$M_{i,g}$	mass of gas components produced by gas-gas reaction	$kg \cdot m^{-3} \cdot s^{-1}$
n	number of coke breezes per unit volume	m^{-3}
Q_{ss}	heat of gas-solid reaction entering solid phase	J
Q_{sg}	heat of gas-solid reaction entering gas phase	J
Q_{conv}	heat of convection	J
R_g	universal gas constant	$J \cdot mol^{-1} \cdot K^{-1}$
r_0	initial radius of coke breezes	m
r_c	un-reacted part radius of coke breezes	m
S	specific surface area	$m^2 \cdot m^{-3}$
T_1	solidus temperature of the melting phase	K
T_2	liquidus temperature of the melting phase	K
T_s	solid phase temperature of the sintering bed	K
T_{max}	highest temperature of sintering process	K
t	time	s
$U_{i,g}$	gas apparent velocity	$m \cdot s^{-1}$
$X_{i,g}$	mass fraction of gas components	–

$\beta_{\text{H}_2\text{O}}$	mass transfer coefficient	$\text{m}\cdot\text{s}^{-1}$
ε	porosity of the bed	–
ε_0	initial porosity of the bed	–
ϕ	shape coefficient	–
ϕ_0	shape coefficient before melting	–
ϕ_1	shape coefficient at the end of solidification	–
φ	polynomial correlation of the characteristic drying curve for iron ore particles	–
$\lambda_{\text{g,eff}}$	effective thermal conductivity of the gas	–
$\lambda_{\text{s,eff}}$	effective heat conduction of solid phase	–
λ_{max}	maximum bed shrinkage rate	–
μ_{g}	dynamic viscosity coefficient	$\text{Ns}\cdot\text{m}^{-2}$
ρ_{g}	gas density	$\text{kg}\cdot\text{m}^{-3}$
ρ_{s}	solid density	$\text{kg}\cdot\text{m}^{-3}$
ρ_{c}	density of coke	$\text{kg}\cdot\text{m}^{-3}$

References

- Jin, L.Z.; Niu, X.M. Micromorphology and safety properties of meager and meager-lean coal for blast furnace injection. *Int. J. Miner. Metall. Mater.* **2021**, *28*, 774–781. [[CrossRef](#)]
- Gao, Q.J.; Wang, H.; Pan, X.Y.; Jiang, X.; Zheng, H.Y.; Shen, F.M. A forecast model of the sinter tumble strength in iron ore fines sintering process. *Powder Technol.* **2021**, *390*, 256–267. [[CrossRef](#)]
- Xiang, D.W.; Shen, F.M.; Yang, J.L.; Jiang, X.; Zheng, H.Y.; Gao, Q.J.; Li, J.X. Combustion characteristics of unburned pulverized coal and its reaction kinetics with CO₂. *Int. J. Miner. Metall. Mater.* **2019**, *26*, 811–821. [[CrossRef](#)]
- Gao, Q.J.; Xie, J.F.; Zhang, Y.Y.; Bao, L.; Zhou, H.Y.; Ye, H.D. Mathematical modeling of natural gas injection in iron ore sintering process and corresponding environmental assessment of CO₂ mitigation. *J. Clean. Prod.* **2021**, *332*, 130009. [[CrossRef](#)]
- Castro, J.; Pereira, J.L.; Guilherme, V.S.; Rocha, E.P.; France, A. Model predictions of PCDD and PCDF emissions on the iron ore sintering process based on alternative gaseous fuels. *J. Mater. Res. Technol.* **2013**, *2*, 323–331. [[CrossRef](#)]
- Meng, C. *Numerical Simulation and Analysis of Sintering Process Using Gas Fuel*; Northeastern University: Shenyang, China, 2016.
- Nobuyuki, O.; Iwami, Y.; Machida, S.; Higuchi, T.; Yamamoto, T.; Watanabe, Y.; Sato, M.; Takeda, K.; Shimizu, M.; Nishioka, K. Reduction of CO₂ emissions with gas fuel injection technology in the sintering machines. *World Iron Steel.* **2013**, *5*, 16–22.
- Wu, Y.; Li, X.J.; Zhang, X.P. Research on visualization technology of gas fuel uniformity in sintering injection. In Proceedings of the 12th China Iron and Steel Annual Conference, Beijing, China, 15 October 2019.
- Wang, G.; Wen, Z.; Lou, G.F.; Dou, R.F.; Li, X.W.; Liu, X.L.; Su, F.Y. Mathematical modeling and combustion characteristic evaluation of a flue gas recirculation iron ore sintering process. *Int. J. Heat Mass Transf.* **2016**, *97*, 964–974. [[CrossRef](#)]
- Ni, W.J.; Li, H.F.; Shao, L.; Zou, Z.S. Numerical simulation on influence of coke oven gas injection on iron ore sintering. *ISIJ Int.* **2020**, *60*, 662–673. [[CrossRef](#)]
- Zhou, H.Y.; Fan, X.H.; Li, Q.; Gan, M. Effect of hydrogen gas injection on the emission of pollutants in sintering. *J. Northeast. Univ. (Nat. Sci.)*. **2021**, *42*, 260–267.
- Feoktistov, A.V.; Odintsov, A.A. Making more efficient use of solid fuel in two-layer sintering. *Metallurgist* **2014**, *58*, 469–477. [[CrossRef](#)]
- Petrushev, S.n.; ayebedev, V.a.; Zhang, Z.Y. Regulation of segregation of sintering fabric. *Sinter. Pelletizing* **1984**, *9*, 109–111.
- Zhou, M.S.; Wang, Y.D.; Han, S.F.; Zhao, D.M.; Zhu, J.W.; Zhong, Q.; Jiang, T. Study on double-layer pre-sintering process of ultra-thick layer. *Sinter. Pelletizing* **2019**, *44*, 23–27.
- Xu, H. *Intelligent Optimal Control System for Sintering Segregation*; Central South University: Changsha, China, 2013.
- Young, R.W. Dynamic mathematic model of sintering progress. *Ironmak. Steelmak.* **1977**, *4*, 321–328.
- Vizureanu, P.; Agop, M. A Theoretical Approach of the Heat Transfer in Nanofluids. *Mater. Trans.* **2007**, *48*, 3021–3023. [[CrossRef](#)]
- Oyama, N.; Iwami, Y.; Yamamoto, T.; Machida, S.; Higuchi, T.; Sato, H.; Sato, M.; Takeda, K.; Watanabe, Y.; Shimizu, M. Development of secondary-fuel injection technology for energy reduction in iron ore sintering process. *Tetsu-to-Hagané* **2011**, *97*, 510–518. [[CrossRef](#)]
- Ramos, M.V.; Kasai, E.; Kano, J.; Nakamura, T. Numerical simulation model of the iron ore sintering process directly describing the agglomeration phenomenon of granules in the packed bed. *ISIJ Int.* **2000**, *40*, 448–454. [[CrossRef](#)]
- Yang, W.; Ryu, C.; Choi, S.; Choi, E.; Lee, D.; Huh, W. Modeling of combustion and heat transfer in an iron ore sintering bed with considerations of multiple solid phases. *ISIJ Int.* **2004**, *44*, 492–499. [[CrossRef](#)]
- Castro, J.; Sazaki, Y.; Yagi, J. Three dimensional mathematical model of the iron ore sintering process based on multiphase theory. *Mater. Res.* **2012**, *15*, 848–858. [[CrossRef](#)]
- Kasai, E.; Yagi, J.; Omori, Y. Mathematical modelling of sintering process considering the influence of changes in void fraction and apparent particle size in the bed on pressure drop. *Tetsu-to-Hagané* **1984**, *70*, 1567–1574. [[CrossRef](#)]
- Ahn, H.; Choi, S.; Cho, B. Process simulation of iron ore sintering bed with flue gas recirculation, Part 1—Modelling approach. *Ironmak. Steelmak.* **2013**, *40*, 120–127. [[CrossRef](#)]

24. Ahn, H.; Choi, S.; Cho, B. Process simulation of iron ore sintering bed with flue gas recirculation, Part 2—Parametric variation of gas conditions. *Ironmak. Steelmak.* **2013**, *40*, 128–137. [[CrossRef](#)]
25. Tiwari, H.P.; Das, A.; Singh, U. Novel technique for assessing the burnout potential of pulverized coals/coal blends for blast furnace injection. *App. Therm. Eng.* **2018**, *130*, 1279–1289. [[CrossRef](#)]
26. Ni, W.J.; Li, H.F.; Zhang, Y.; Zou, Z. Effects of fuel type and operation parameters on combustion and NO_x emission of the iron ore sintering process. *Energies* **2019**, *12*, 213. [[CrossRef](#)]
27. Giri, B.K.; Roy, G.G. Mathematical modelling of iron ore sintering process using genetic algorithm. *Ironmak. Steelmak.* **2012**, *39*, 59–66. [[CrossRef](#)]
28. Zhao, J.; Loo, C.; Dukino, R. Modelling fuel combustion in iron ore sintering. *Combust. Flame.* **2014**, *162*, 1019–1034. [[CrossRef](#)]
29. Cheng, Z.; Wei, S.; Guo, Z.; Yang, J.; Wang, Q. Improvement of heat pattern and sinter strength at high charcoal proportion by applying ultra-lean gaseous fuel injection in iron ore sintering process. *J. Clean. Prod.* **2017**, *161*, 1374–1384. [[CrossRef](#)]
30. Nath, N.; Mitra, K. Mathematical modeling and optimization of two-layer sintering process for sinter quality and fuel efficiency using genetic algorithm. *J. Mater. Manuf. Process.* **2005**, *20*, 335–349. [[CrossRef](#)]
31. Loo, C.; Tame, N.; Penny, G. Effect of iron ores and sintering conditions on flame front properties. *ISIJ Int.* **2012**, *52*, 967–976. [[CrossRef](#)]
32. Zhang, Z.; Ai, L.G. *Mathematical Analysis and Simulation of Metallurgical Process*; Metallurgical Industry Press: Beijing, China, 1997.
33. Liu, B.; Feng, Y.H.; Jiang, Z.Y. Heat and mass transfer in sintering process. *CIESC J.* **2012**, *63*, 1344–1353.